Ion kinetics in the solar wind: coupling global expansion to local microphysics

Lorenzo Matteini · Petr Hellinger · Simone Landi · Pavel M. Trávníček · Marco Velli

Abstract We discuss selected ion kinetic processes relevant in the context of the expanding solar wind. We focus on the role of wave-wave and wave-particle interactions, plasma instabilities and Coulomb collisions on the overall kinetic evolution of ions. We review recent results from the hybrid expanding box model, which enables to couple the large scale effects of the solar wind expansion to the microscale kinetics of ions. We discuss how different plasma processes develop and influence each other during the expansion, as well their role in the shaping of ion distribution functions, and we compare the simulation results with the observed trends in the solar wind.

1 Introduction

The solar wind plasma is only weakly collisional, Coulomb collisions are not able to keep the system at the thermodynamic equilibrium. Coulomb collisions are more important

L. Matteini
Dipartimento di Fisica e Astronomia, Università di Firenze
Largo Enrico Fermi 2, 50125 Florence, Italy
E-mail: matteini@arcetri.astro.it

P. Hellinger
Astronomical Institute and Institute of Atmospheric Physics, AS CR,
Bocni II/1401, 14131 Prague, Czech Republic

S. Landi
Dipartimento di Fisica e Astronomia, Università di Firenze
Largo Enrico Fermi 2, 50125, Florence, Italy

P. M. Trávníček
SSL, University of Berkeley, 7 Gauss Way, Berkeley, CA 94720, U.S.A. &
Astronomical Institute and Institute of Atmospheric Physics, AS CR,
Bocni II/1401, 14131 Prague, Czech Republic

M. Velli
Dipartimento di Fisica e Astronomia, Università di Firenze
Largo Enrico Fermi 2, 50125, Florence, Italy &
JPL, California Institute of Technology, 4800 Oak Grove Drive, Pasadena, CA 91109, U.S.A.

for electrons (e.g., Salem et al. 2003; Štverák et al. 2008; Landi et al. 2010) than for protons, alpha particles and minor ions. While collisions also influence the evolution of ion distribution functions in the slow solar wind (Livi et al. 1986; Livi and Marsch 1986, 1987; Kasper et al. 2008; Bale et al. 2009), their influence seems to be negligible in the fast solar wind (Marsch 2006). Far from the thermodynamic equilibrium the solar wind plasma often contains a free energy for driving macro- and micro-instabilities and magnetohydrodynamic, as well as kinetic plasma waves and associated wave-particle and wave-wave interactions are expected to play an important role. Moreover, the solar wind exhibits large and developed electromagnetic wave activity/turbulence.

Remote SOHO spacecraft observations of strong temperature anisotropies of minor ions (Kohl et al. 1998; Li et al. 1998; Telloni et al. 2007) indicate an efficient heating perpendicular with respect to the ambient magnetic field. A natural source of such a heating is the cyclotron resonance with Alfvén cyclotron waves (Hollweg and Isenberg 2002). Also in situ observations show that the ion velocity distribution functions in the solar wind typically exhibit large departures from isotropic (Maxwellian) distribution functions. They are usually anisotropic (with different parallel and perpendicular temperatures with respect to the ambient magnetic field). The proton distribution functions often exhibit a structure with a core and a pronounced magnetic field-aligned beam with a number density of the order of tenths of the core density and with the beam/core relative velocity of the order of the local Alfvén velocity (Marsch et al. 1982a). The minor ions are typically hotter than protons and have also a drift velocity (with respect to the proton core) of the order of the local Alfvén velocity (Marsch et al. 1982b). The evolution of the ion velocity distributions from 0.3 AU beyond 1 AU does not follow either collisionless double adiabatic or collisional adiabatic predictions. The total proton temperature decreases slower than what is predicted by the adiabatic approximation indicating some heating processes. On the other hand, the perpendicular temperature decreases slower than what is expected from the double-adiabatic approximation whereas the parallel temperature decreases faster. Moreover, the drift velocities between the core protons and the proton beam/alpha particles decrease following the local Alfvén velocity. Some of these properties are compatible with the interaction of the ions with high frequency Alfvén cyclotron waves with ions (cf., Hollweg and Isenberg 2002). Indications of cyclotron heating signatures, formation of the cyclotron quasilinear plateaux, are also reported (Heuer and Marsch 2007). However, the cyclotron resonance and other mechanisms which form and regulate the ion distribution functions are not fully understood. In situ observations show that different characteristic parameters of the proton distribution functions are correlated (Marsch et al. 2004; Tu et al. 2004; Gary et al. 2005, 2006) but the origin of these correlations is not clear. They may be related to wave-particle interactions associated with the heating processes and/or due to other plasma processes as kinetic instabilities.

The frequency distribution of the observed proton temperature anisotropy in the solar wind exhibits phenomenological bounds. These bounds are compatible with theoretical stability limits set by plasma instabilities predicted by the linear analysis (Gary et al. 2001; Kasper et al. 2002; Hellinger et al. 2006; Marsch et al. 2006; Matteini et al. 2007), suggesting that these instabilities are active in the solar wind plasma and constrain the values of the observed anisotropies. Indications of similar instability constraints on the temperature anisotropy are also observed for alpha particles (Maruca et al. 2009). Analogous phenomenological bounds, compatible with the theoretical instability limits for electron temperature anisotropies (Gary and Madland 1985; Li and Habbal 2000; Camporeale and Burgess 2008), are observed for the solar wind electrons
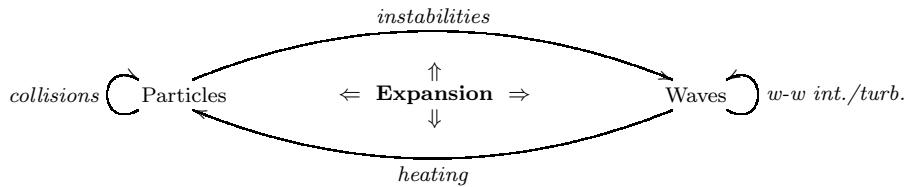
Fig. 1 Schematic view of energy exchanges in a plasma. The sense of arrows indicate the direction of the energy transfer. Expansion influences interactions between waves and particles.

(Gary et al. 1999; Štverák et al. 2008). Furthermore, observations of an enhanced power of magnetic fluctuations near the instability thresholds set by the proton temperature anisotropy driven instabilities (Bale et al. 2009) suggest that the instabilitity driven waves are indeed present and active. Observational bounds suggesting instability constraints on the differential velocity between the proton core and beam have been also identified (Marsch and Livi 1987; Tu et al. 2004; Goldstein et al. 2000; Goldstein et al. 2010); moreover, possible constraints on the differential velocity between the proton core and alpha particles are also reported (Tu et al. 2004).

Detailed comparisons between observations and the theoretical (linear) predictions allow in principle to identify the relevant mechanisms/instabilities constraining the solar wind plasma; however, one has to consider that different processes can concur/compete. On one side, accurate and high resolution data are needed to infer the dominant processes from observations, and, on the other side, it is important to go beyond the linear approximation in the theoretical analysis. First, the linear predictions are quite limited as the full parameter space for the linear analysis has many dimensions (i.e., density, temperatures and velocity for each species), and, second, one has to take into account their nonlinear evolution, especially when dealing with a dynamic system where a source of instability is continuously driven (e.g., due to the solar wind expansion and/or wave-particle interactions). For these reasons, numerical simulations are needed in order to catch the complexity and the full non-linear evolution of the plasma.

Schematic view of the different interactions in the solar wind (not restricted to ions) is shown in Figure 1. Different processes lead to: energy exchanges between particles (collisions), interactions between different wave modes (wave-wave interactions or turbulence), as well as energy exchanges between waves and particles. In the figure the sense of the arrows indicate the direction of the energy flow: from waves to particles in case of wave damping and plasma heating, and from particles to waves in case of kinetic microinstabilities. The relative importance of these effects depends on the plasma conditions and can vary largely during the solar wind evolution with the radial distance. A crucial point in the understanding of how kinetic processes act in the solar wind is then to include the effects of the plasma expansion. The spherical expansion modifies the characteristic particle spacial and temporal scales, drives the evolution of the particle distribution functions, and changes the magnitude of the ambient magnetic field as well as energies in the wave-modes.

In this review we focus on kinetic processes related to the nonthermal ion features in the expanding solar wind, their origins and consequences. Note that similar issues have to be considered also for electrons, although their relative importance may

be different compared to ions. Section 2 describes theoretical expectations of the ion evolution in a collisionless radially expanding solar wind plasma. Section 3 discusses the effect of Coulomb collisions on the ion evolution. Section 4 deals with proton temperature anisotropy and alpha-proton drift velocity driven instabilities and their consequences. Section 5 discusses the ion heating by high frequency Alfvén cyclotron waves and section 6 deals with the parametric instabilities of large amplitude Alfvén waves. In section 7 we discuss the different kinetic processes, their relationship and their consequences.

2 Double adiabatic prediction for the radial evolution

Particle evolution in a spherically expanding collisionless plasma can be simply modeled assuming conservation of the magnetic moment $v_\perp^2/B$ (see appendix for symbol definitions) and of the total kinetic energy $v_\parallel^2 + v_\perp^2$ for each particle. In this model we assume a strictly radial magnetic field which decreases with the radial distance R as $B = B_0(R_0/R)^2$ (R_0 being the initial radial distance) and a constant radial solar wind velocity v_{sw}. At R_0 we assume a drifting Maxwellian (proton) distribution with a thermal velocity $v_{th\mathrm{p}}$ much smaller than the initial drift velocity v_{sw} (in the Sun rest frame). The conservation of the magnetic moments imposes $v_\perp \propto 1/R$ and the lost perpendicular energy is transformed into the parallel one. Results of such a simple model are shown in Figure 2 for $v_{sw}/v_{th\mathrm{p}} = 8$. Left panel of Figure 2 shows the final proton distribution function at $R = 3R_0$ by the color scale; the initial distribution at R_0 is indicated by dashed contours. The modeled expansion leads to a significant particle temperature anisotropy. Right panels display the evolution of parallel (solid line) and perpendicular (dashed line) temperatures (top right) and mean velocity (bottom right) as a function of the relative distance R. The model predicts a strong decrease of the perpendicular temperature which decreases as $1/R^2$ while the parallel temperature remains about constant. The mean proton velocity $v_{\mathrm{s}\parallel}$ remains also about constant, given the negligible contribution of the mirror force. A similar temperature evolution, with the development of a strong $T_\parallel > T_\perp$ anisotropy, is generally observed in kinetic solar wind models which include the regulation of the mean flow velocity via the interplanetary electric field (e.g., Lemaire and Scherer 1971), even when other ingredients, such as Coulomb collisions (Landi and Pantellini 2003), non-radial magnetic field (Pierrard et al. 2001), or non-thermal electron distribution functions (Zouganelis et al. 2005), are included.

The results of the simple microscopic model described above are compatible with the macroscopic fluid description. In this framework, evolution of parallel and perpendicular temperatures in collisionless plasmas maybe described at lowest order (neglecting collisions and heatfluxes) by a double-adiabatic (or CGL) system of equations (Chew et al. 1956) based on two adiabatic invariants $T_\perp/B$ and $T_\parallel B^2/n^2$. Conservation of the two adiabatic invariants leads to an evolution of the parallel and perpendicular temperatures, $T_\parallel$ and $T_\perp$, as:

$$\left(\frac{\mathrm{d}T_\parallel}{\mathrm{d}t}\right)_{\mathrm{CGL}} = 2\frac{T_\parallel}{n}\frac{\mathrm{d}n}{\mathrm{d}t} - 2\frac{T_\parallel}{B}\frac{\mathrm{d}B}{\mathrm{d}t} \quad \text{and} \quad \left(\frac{\mathrm{d}T_\perp}{\mathrm{d}t}\right)_{\mathrm{CGL}} = \frac{T_\perp}{B}\frac{\mathrm{d}B}{\mathrm{d}t} \ . \tag{1}$$

For a spherical expansion in the presence of a strictly radial magnetic field and a constant (radial component of the) solar wind velocity (e.g., the polar solar wind
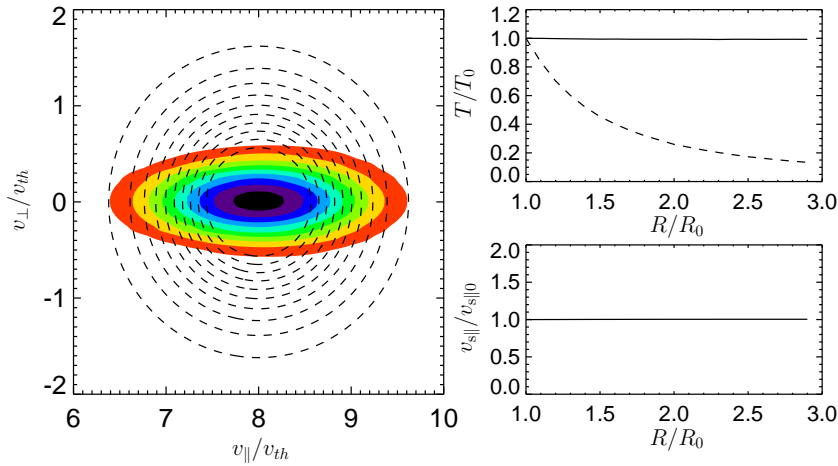
Fig. 2 Evolution of ion distribution in the case of a supersonic expansion with $v_{sw} = 8v_{th\mathrm{p}}$. (left) Color scale plot shows the final velocity distribution function f as a function of $v_\parallel$ and $v_\perp$ at $R = 3R_0$; the initial bi-Maxwellian distribution at $R_0 = 1$ is reported in dashed contours. Right panels: (top) parallel (solid line) and perpendicular (dashed line) temperatures, and (bottom) mean flow velocity.

in a first approximation) where the magnitude of the magnetic field and the particle density decrease with the distance R as B, $n \propto R^{-2}$, then Eq. (1) predicts the following evolution of the proton parallel and perpendicular temperatures:

$$T_{\mathrm{p}\perp} \propto R^{-2} \qquad \text{and} \qquad T_{\mathrm{p}\parallel} = \text{const} . \tag{2}$$

Note that for $T_\parallel = T_\perp = T$ we have

$$\left(\frac{\mathrm{d}T}{\mathrm{d}t}\right)_{\mathrm{CGL}} = \frac{2}{3}\frac{T}{n}\frac{\mathrm{d}n}{\mathrm{d}t} \tag{3}$$

leading to the well known adiabatic temperature radial profile

$$T \propto R^{-4/3} , \tag{4}$$

for the adiabatic spherical expansion of a gas with the adiabatic index $\gamma = 5/3$ (e.g., Verma et al. 1995; Williams et al. 1995). However this assumes the presence of a mechanism, like collisions, that keeps particles isotropic (Maxwellian). In the absence of such an efficient mechanism and if $T_\parallel \neq T_\perp$, Eq. (1) should instead be used to describe the evolution of the system. This is the case of the expanding solar wind once the solar wind has reached its supersonic steady regime (Schulz and Eviatar 1973). However, the ideal CGL/double-adiabatic evolution is altered by the presence of collisions, significant heat fluxes, and kinetic effects.

From the double-adiabatic assumption, in a strictly radial magnetic field, we have the evolution of the parallel beta:

$$\beta_{\mathrm{p}\parallel} \propto \frac{nT_{\mathrm{p}\parallel}}{B^2} \propto R^2 \propto T_{\mathrm{p}\parallel}/T_{\mathrm{p}\perp}. \tag{5}$$

The evolution of protons predicted by the CGL approximation can be then compared to direct solar wind observations. Figure 3 reports Helios histograms of the observational
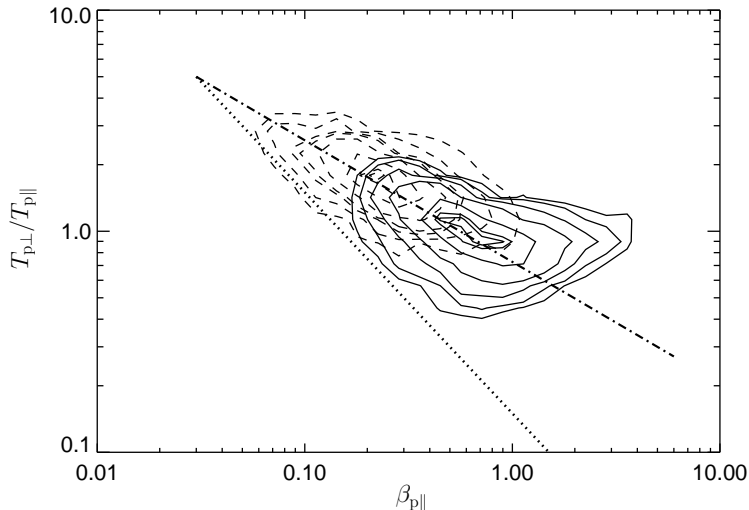
Fig. 3 Evolution of proton temperature anisotropy in the solar wind from Helios observations (Matteini et al. 2007): Contours of the observed frequency of $\beta_{p\parallel}$ $T_{p\perp}/T_{p\parallel}$ at (dashed) 0.3 AU and (solid) 1 AU. Dotted lines displays the CGL predictions for a strictly radial magnetic field $T_{p\perp}/T_{p\parallel} \propto 1/\beta_{p\parallel}$. Dash-dotted line shows the empirical anti-correlation inferred by data between 0.3 and 1 AU (Marsch et al. 2004).

counts of $(\beta_{p\parallel}, T_{p\perp}/T_{p\parallel})$ in the fast wind at 0.3 (dashed) and 1 (solid) AU (adapted from Matteini et al. 2007). The radial evolution of the observed $(\beta_{p\parallel}, T_{p\perp}/T_{p\parallel})$ follows a path encoded by the dash-dotted line (Marsch et al. 2004); the observed anti-correlation $\beta_{p\parallel}$-$T_{p\perp}/T_{p\parallel}$ departs from the CGL prediction, reported by the dotted line. This suggests that some (perpendicular) heating is at work between 0.3 and 1 AU, contrasting the predicted strong cooling of $T_{p\perp}$. It is interesting to note that the slope of the CGL prediction (Figure 3, dotted line) constitutes a sort of lower boundary for the observations; although this can be a mere coincidence; a steeper path in the $(\beta_{p\parallel}, T_{p\perp}/T_{p\parallel})$ space than the CGL one would imply a (perpendicular) proton cooling which seems to be excluded by observations.

On the other hand, for $\beta_{p\parallel} > 1$ data show a departure from the empirical correlation observed at lower $\beta_{p\parallel}$. As we will discuss in next sections, this is related to the fact that for $\beta_{p\parallel} > 1$ anisotropic plasma with $T_{p\parallel} > T_{p\perp}$ can develop fire hose instabilities; this is likely to happen in the solar wind since the observed trend (dashed line in Figure 3) would drive large $T_{p\parallel} > T_{p\perp}$ anisotropies with increasing $\beta_{p\parallel}$ and making then the plasma unstable. As a feedback, fluctuations excited by the instability reduce the proton anisotropy and force the system to a more isotropic state, in agreement with the data for $\beta_{p\parallel} > 1$ where $T_{p\perp}/T_{p\parallel} \sim 1$. Ulysses observations at larger distances (2-3 AU) confirm this picture (Matteini et al. 2007)

Another consequence of relations (1) concerns the parallel velocities of each species, $v_{s\parallel}$. Their evolution in the absence of collisions is

$$\left(\frac{dv_{s\parallel}}{dt}\right)_{CGL} = \frac{v_{s\parallel}}{n}\frac{dn}{dt} - \frac{v_{s\parallel}}{B}\frac{dB}{dt}. \qquad (6)$$

For the strictly radial magnetic field Eq. (6) predicts constant parallel velocities of each species, $v_{s\parallel} =$ const as well as constant parallel drift velocities between the different

species. On the other hand, the Alfvén velocity evolves with distance as $v_A \propto B/\sqrt{n}$. For a strictly radial magnetic field Alfvén velocity decreases as $v_A \propto R^{-1}$. Consequently, the ratio between the parallel drift velocities and the local Alfvén velocity is expected to increase with distance (for a nearly radial magnetic field), giving rise to a free energy for beam-type instabilities.

These two examples suggest how common non-thermal features observed in the solar wind, temperature anisotropies and particle beams, are governed by the expansion, and can naturally develop instabilities that play a role in the overall dynamics of the plasma and importantly change the energetics of the system.

Collisions and a non strictly radial magnetic field can introduce departures from the simple scaling described above for the strictly radial field. For example, in the case of a spiral magnetic field (Parker 1958) we have for the radial and tangential components of the magnetic field, $B_r \propto R^{-2}$ and $B_t \propto R^{-1}$, respectively, predicting then an evolution for temperatures departing from (2). The role of collisions is studied in the next section for both the radial and Parker spiral field geometries.

3 Coulomb collisions

The solar wind plasma is generally far from the thermodynamic equilibrium. Different species have different, often anisotropic temperatures and different velocities. The standard collisional transport coefficients (Spitzer and Härm 1953; Braginskii 1965) are in the solar wind context questionable (cf., Landi and Pantellini 2001, 2003). Collisional transport in anisotropic bi-Maxwellian plasmas has been studied by Barakat and Schunk (1981) and recently by Hellinger and Trávníček (2009) who derived the anisotropic transport coefficients in a closed form involving double hypergeometric functions. Two specific transport coefficients are considered here:

– the isotropization rate due to proton-proton collisions

$$\left(\frac{\mathrm{d}T_{\mathrm{p}\perp}}{\mathrm{d}t}\right)_{\mathrm{coll}} = -\frac{1}{2}\left(\frac{\mathrm{d}T_{\mathrm{p}\parallel}}{\mathrm{d}t}\right)_{\mathrm{coll}} = -\nu_T\left(T_{\mathrm{p}\perp} - T_{\mathrm{p}\parallel}\right) \tag{7}$$

where the isotropization frequency ν_T maybe given (Kogan 1961; Hellinger and Trávníček 2009):

$$\nu_T = \frac{e4n_{\mathrm{p}}\ln\Lambda}{30\pi^{3/2}\epsilon_0^2 m_{\mathrm{p}}^2 v_{th\mathrm{p}\parallel}^3}\ {}_2F_1\left(\begin{array}{c}2,3/2\\7/2\end{array};1-\frac{T_{\mathrm{p}\perp}}{T_{\mathrm{p}\parallel}}\right)\ , \tag{8}$$

$_2F_1$ being the standard (Gauss) hypergeometric function.

– the slowing down of alpha particles with respect to the (core) protons

$$\left(\frac{\mathrm{d}v_{\alpha\mathrm{p}}}{\mathrm{d}t}\right)_{\mathrm{coll}} = -\nu_V v_{\alpha\mathrm{p}} \tag{9}$$

where the slowing down frequency ν_V maybe expressed in the terms of double hypergeometric functions (Hellinger and Trávníček 2009).

Following Kasper et al. (2008) and Bale et al. (2009) one can quantify the role of Coulomb collisions in isotropization of protons and in slowing down alpha particles with respect to protons. Figure 4 shows the fitted data from the Faraday cup experiment

on the Wind spacecraft obtained during 1995–2001 (Kasper et al. 2002; Kasper et al. 2006). Left panel of Figure 4 displays a color scale plot of the relative frequency of $\nu_T t_e$ and $T_{\mathrm{p}\perp}/T_{\mathrm{p}\parallel}$ while right panel of Figure 4 displays a color scale plot of the relative frequency of $\nu_V t_e$ and $v_{\alpha\mathrm{p}}/v_A$ for the solar wind with $v_{\mathrm{sw}} \leq 600$ km/s. Here t_e is the characteristic expansion time $t_e = R/v_{\mathrm{sw}}$ at the radial distance $R = 1$ AU. Figure 4 clearly demonstrates that in a more collisional plasma protons are more isotropic and the differential velocity between the alpha particles and protons is smaller. The fast solar wind is much less collisional with $\nu_T t_e \sim \nu_V t_e \sim 10^{-2}$ and no clear role of collisions is observed.
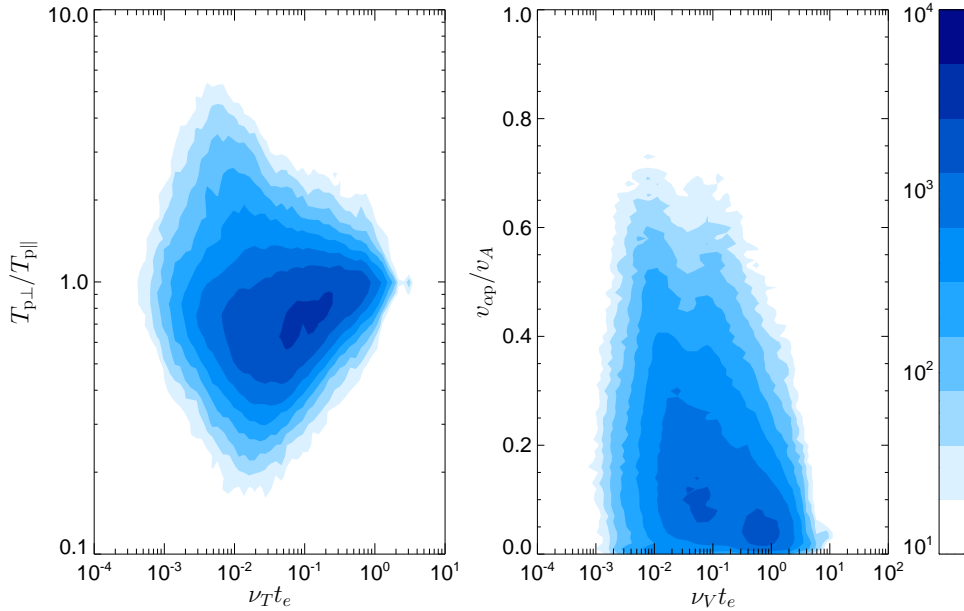

Fig. 4 WIND/SWE observations: (left) Color scale plot of the relative frequency of $\nu_T t_e$ and $T_{\mathrm{p}\perp}/T_{\mathrm{p}\parallel}$ and (middle) color scale plot of the relative frequency of $\nu_V t_e$ and $v_{\alpha\mathrm{p}}/v_A$ for the solar wind with $v_{\mathrm{sw}} \leq 600$ km/s. The (logarithmic) color scale is shown on the right.

The collisional transport in the expanding solar wind plasma far from the thermal equilibrium may be quite complex. Although the final/asymptotic state is described by one (isotropic) temperature and one velocity, intermediate/transient states may vary. A relatively simple evolution is observed for one population of anisotropic protons (here the interaction with electrons is neglected). Figure 5 shows an evolution of weakly collisional system (coupling CGL and anisotropic transport coefficients, cf., Phillips and Gosling 1990) starting with $\beta_{\mathrm{p}\parallel} = 0.2$ and $T_{\mathrm{p}\perp}/T_{\mathrm{p}\parallel} = 2$ with $t_e = 10^4/\omega_{c\mathrm{p}}$ and $\nu_T = 0.1/t_e$ at t_0 (and R_0 assumed to be ~ 0.3 AU). The left top panel shows the total temperature T as a function of R, the right top panel shows the temperature anisotropy $T_{\mathrm{p}\perp}/T_{\mathrm{p}\parallel}$ as a function of R, the left bottom panel shows the parallel beta $\beta_{\mathrm{p}\parallel}$ as a function of R and the right bottom panel shows a path in the $(\beta_{\mathrm{p}\parallel}, T_{\mathrm{p}\perp}/T_{\mathrm{p}\parallel})$ space. Solid lines show the results for the radial magnetic field whereas dashed lines shows the results for a standard Parker spiral model (with an angle of 45 degrees at 1 AU). The dash-dotted line in the top left panel shows the adiabatic prediction, Eq. (4),

whereas the dotted lines in the other panels show the corresponding CGL evolution, Eq. (1). In the radial case a relatively strong temperature anisotropy develops and the total temperature departs significantly from the adiabatic prediction $T \propto R^{-4/3}$; in this case the evolution roughly follows the CGL prediction. In the Parker spiral case the temperature anisotropy is much smaller and the total temperature follows closely the adiabatic prediction; in this case the collisional frequency $\propto n/T^{3/2}$ is about constant while the expansion characteristic time $t_e = R/v_{\mathrm{sw}}$ increases and, consequently, the local collisionality factor $\nu_T t_e$ increases with the time/distance. In contrast, for the strictly radial magnetic field a strong temperature anisotropy develops and $\nu_T t_e$ stays about constant.
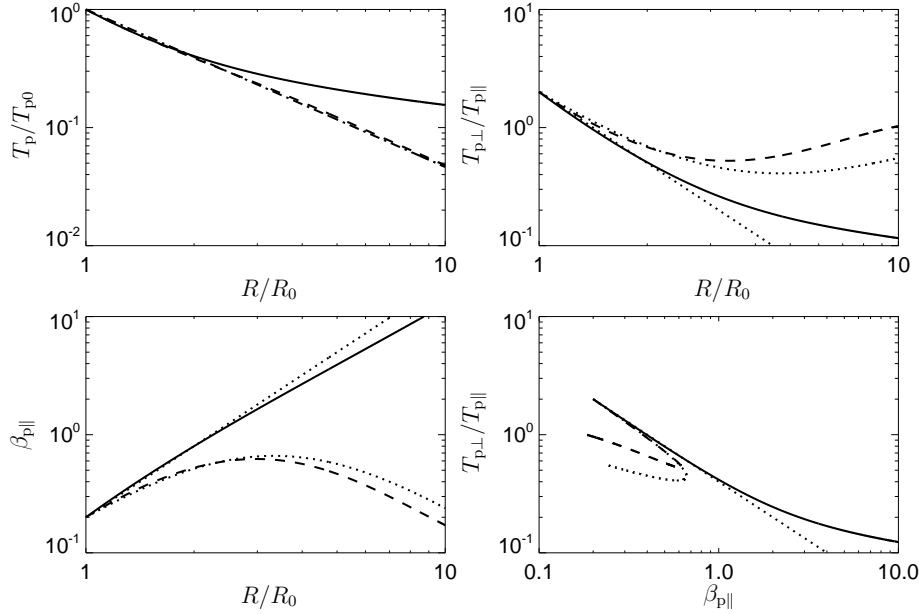
Fig. 5 Weakly collisional protons in the expanding solar wind: (left top) the total proton temperature T as a function of R, (right top) the proton temperature anisotropy $T_{\mathrm{p}\perp}/T_{\mathrm{p}\|}$ as a function of R (left bottom) the parallel beta $\beta_{\mathrm{p}\|}$ as a function of R and (right bottom) the system evolution as a path in the $(\beta_{\mathrm{p}\|}, T_{\mathrm{p}\perp}/T_{\mathrm{p}\|})$ space. Solid lines denote the case of the radial magnetic field whereas dashed lines shows the results the nominal Parker spiral. The dash-dotted line in the top left panel shows the adiabatic prediction, Eq. (4), whereas the dotted lines in the other panels show the corresponding CGL predictions, Eq. (1).

A more complex behavior appears when considering multiple species drifting with respect each other. Figure 6 shows an evolution in a weakly collisional plasma assuming alpha particles drifting along the ambient magnetic field with respect to protons in the case of the strictly radial magnetic field. Only ion-ion collisions are considered, ion-electron collisions are neglected. Initially we set $n_{\mathrm{p}}/n_{\mathrm{e}} = 0.9$, $n_{\alpha}/n_{\mathrm{e}} = 0.05$, $\beta_{\mathrm{p}\|} = 0.2$, $\beta_{\alpha\|} = 0.05$, $T_{\mathrm{p}\perp}/T_{\mathrm{p}\|} = 2$, $T_{\alpha\perp}/T_{\alpha\|} = 1$, and $v_{\alpha\mathrm{p}} = v_A$ with $t_e = 10^4/\omega_{c\mathrm{p}}$ and $\nu_T = 0.1/t_e$ (R_0 is again assumed to be about 0.3 AU). The top left panel of Figure 6 shows the ratio between the alpha-proton drift velocity and the local Alfvén velocity $v_{\alpha\mathrm{p}}/v_A$ as a function of R. The top right panel reports the total (solid) proton and

(dashed) alpha temperature evolution T (normalized to the initial proton temperature T_{p0}) as a function of R. The bottom left panel displays the ratio between the total temperature of alpha particles and that of protons, T_α/T_p as a function of R. The bottom right panel shows the evolution of proton and alpha particle parameters as a path in the $(\beta_\parallel, T_\perp/T_\parallel)$ space. The dotted lines denote the corresponding CGL predictions whereas the dash-dotted lines denote the corresponding adiabatic prediction, Eq. (4). Note that even the CGL/double-adiabatic approximation predicts a nontrivial evolution of T_α/T_p when $T_{p\perp}/T_{p\parallel}$ and $T_{\alpha\perp}/T_{\alpha\parallel}$ are different. Coulomb collisions between the two species lead to the slowing down with respect to each other. The energy associated with the drift between the two species is converted into the thermal energy of each species; alpha particles are predominantly heated (with similar parallel and perpendicular heating rates) whereas protons are heated only weakly and mainly in the perpendicular direction. It is interesting to note that in the absence of the drift between protons and alpha particles Coulomb collisions thermalize the ions, reducing the temperature difference between the two species. When an important velocity drift is present, the collisional coupling has the opposite effect, increasing the temperature ratio T_α/T_p. This collisional differential heating is only transient and disappears when the drift velocity is strongly reduced. This result suggests that the collision coupling may be partly responsible for the observed difference between the proton and alpha-particle temperatures (cf. Kasper et al. 2008).
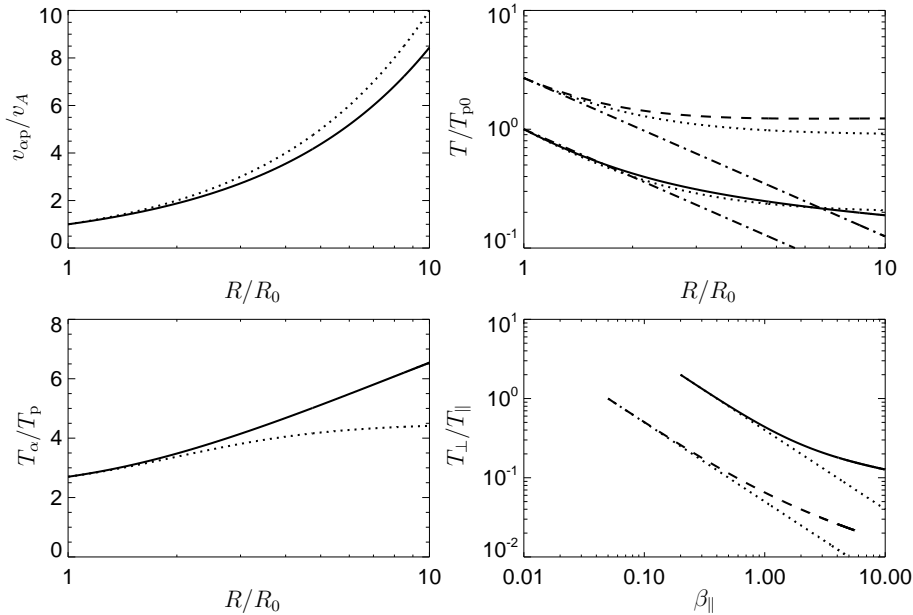
Fig. 6 Weakly collisional alpha-proton system with a relative drift in the expanding solar wind (for the radial magnetic field): (top left) the alpha-proton drift velocity $v_{\alpha p}$ (normalized to v_A) as a function of R, (top right) the total (solid) proton and (dashed) alpha-particle temperatures T_p and T_α (normalized to the initial proton temperature T_{p0}) as functions of R. (bottom left) the temperature ratio T_α/T_p as a function of R, and (bottom right) the evolution of (solid) protons and (dashed) alphas as paths in the $(\beta_\parallel, T_\perp/T_\parallel)$ space. Dotted lines denote the corresponding CGL predictions, Eq. (1), whereas the dash-dotted lines denote the corresponding adiabatic prediction, Eq. (4).

4 Ion instabilities

The solar wind ions have different, typically anisotropic temperatures and different velocities and even exhibit secondary (beam) populations. Temperature anisotropies and differential velocities between the different species/populations are sources of free energy for many electromagnetic and electrostatic instabilities. One important, relatively general result on ion instabilities have been established (Gary 1993): Ion or ion-ion electromagnetic instabilities are generally the most robust ones, and may grow to higher amplitudes than the ion-electron electromagnetic and electrostatic instabilities even if the latter have generally higher growth rates.

4.1 Temperature anisotropy

The presence of strong proton temperature anisotropies in the solar wind is well established. For example, Hellinger et al. (2006) compared the statistically large dataset of the Wind/SWE (Kasper et al. 2002; Kasper et al. 2006) with the predictions of the Vlasov linear theory (for a plasma consisting of Maxwellian electrons and bi-Maxwellian protons) considering four distinct electromagnetic instabilities: proton cyclotron, mirror, parallel and oblique fire hose instabilities. In the slow solar wind, the observed proton temperature anisotropy seems to be constrained by the oblique instabilities (the mirror one and oblique fire hose) in an apparent contradiction with the results of the linear theory which predicts that the proton cyclotron instability and of the parallel fire hose would dominate for all but large proton betas. This contradiction is likely related to the limitation of the linear model (simplified plasma composition adopted for the linear analysis) and to the presence of nonlinear effects (see discussion in Hellinger et al. 2006). For instance, the presence of alpha particles importantly modifies the proton cyclotron instability while only weakly affects the mirror instability (Price et al. 1986). This effect is clearly demonstrated in Figure 7 which shows the color scale plots of the relative frequency of $\beta_{p\parallel}$ and $T_{p\perp}/T_{p\parallel}$ for the solar wind with $v_{sw} \leq 600$ km/s (cf., Hellinger et al. 2006, Figure 1). The (logarithmic) color scale is shown on the right. The over plotted curves show the contours of the maximum growth rate (in units of ω_{cp}) over the range of unstable wavevectors as a function of $\beta_{p\parallel}$ and anisotropy, in the corresponding bi-Maxwellian plasma. Left panel reports the proton cyclotron instability (solid curves) and the parallel fire hose (dashed curves) and right panel the mirror instability (dotted curves) and the oblique fire hose (dash-dotted curves). In all cases a 5 % composition of alpha particles is considered in the plasma; alpha particles are assumed to be isotropic with the temperature equal to the proton parallel temperature and alpha-proton drift velocity is zero. Figure 7 shows that even when considering alpha-particle parameters as ad-hoc functions of the proton ones the agreement between the linear prediction for the proton cyclotron instability and the solar wind data improves considerably. This suggests that the comparison between the linear prediction and the observed data needs as good as possible plasma description, since in principle all the parameters, as the plasma composition, temperature ratios, anisotropies and drift velocities of each species, can introduce major effects in the dispersion and should be taken into account in the computation of linear stability. However, taking for the solar wind ions only alpha particle and protons consisting of a core and beam, assuming for simplicity drifting bi-Maxwellian velocity distribution

functions, we already deal with too many parameters to investigate, making such a theoretical approach unfeasible (cf., Hellinger et al. 2005).
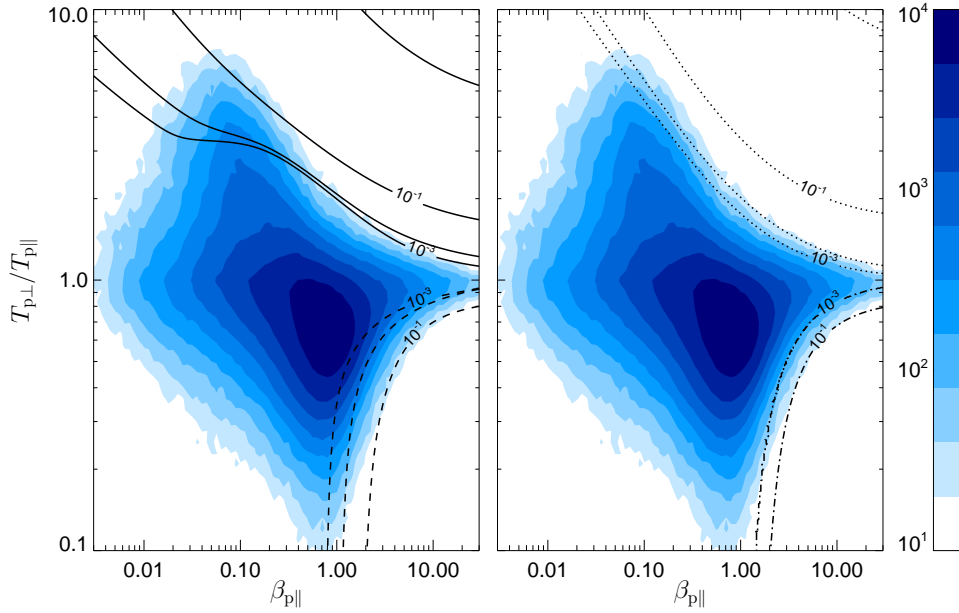
Fig. 7 WIND/SWE observations: color scale plots of the relative frequency of $\beta_{\mathrm{p}\parallel}$ and $T_{\mathrm{p}\perp}/T_{\mathrm{p}\parallel}$ for the solar wind with $v_{\mathrm{sw}} \leq 600$ km/s. The (logarithmic) color scale is shown on the right. The over plotted curves show the contours of the maximum growth rate (in units of ω_{cp}) in the corresponding bi-Maxwellian plasma (left) for the proton cyclotron instability (solid curves) and the parallel fire hose (dashed curves) and (right) for the mirror instability (dotted curves) and the oblique fire hose (dash-dotted curves) with 5 % of alpha particles.

4.2 Hybrid expanding box

To investigate the role of nonlinear kinetic effects one has to resort to numerical simulations. For the ion physics the electron kinetics is in the first approximation negligible but ions have to be described using a fully self-consistent kinetic manner. This is the base for the so called hybrid approximation where ions are treated as macro-particles within a particle-in-cell model and electrons considered as a massless, charge neutralizing fluid (here we assume a constant temperature). In standard simulations of kinetic instabilities the system starts in the unstable region and the simulation allows to study the nonlinear saturation of the instability. In the solar wind the system starts in the stable region and the expansion and/or wave-particle interactions drive the temperature anisotropy or other sources of free energy for kinetic instabilities (cf., Matteini et al. 2007). To study the response of the plasma to a slow expansion one can use the expanding box model (Grappin et al. 1993) implemented to the hybrid code (Matthews 1994). The Hybrid Expanding Box (HEB) simulations can model the expansion driven anisotropization and wave-particle interactions.

In the expanding box model the solar wind is assumed to have a constant radial velocity v_{sw}. The simulation box is co-moving with the plasma, the radial dependence is replaced by the temporal evolution

$$R = R_0 + v_{sw}t = R_0(1 + t/t_e) \qquad (10)$$

where $t_e = R_0/v_{sw}$ is the (initial) characteristic expansion time (cf., Hellinger and Trávníček 2005, for a detailed description of the code). Transverse scales increase with time $\propto R \propto (1 + t/t_e)$ while the density decreases as R^{-2}; the radial component of the magnetic field decreases as R^{-2} whereas the transverse components decrease as R^{-1}. In the absence of collisions and wave-particle couplings ions follow the CGL/double-adiabatic prediction, while in the absence of dissipation/damping and wave-wave interactions the model predicts the WKB evolution of waves (Liewer et al. 2001; Hellinger et al. 2005).

The competition between the expansion and the fire hose instabilities was studied using the HEB model in the collisionless plasma by Matteini et al. (2006) and Hellinger and Trávníček (2008) and by Hellinger and Trávníček (2010) who included weak Coulomb collisions through the Langevin stochastic equation corresponding to the Fokker-Planck equation. The evolution of the weakly collisional HEB simulations with the initial conditions $T_{\mathrm{p}\perp}/T_{\mathrm{p}\parallel} = 0.4$, $\beta_{\mathrm{p}\parallel} = 0.3$, $t_e = 10^4/\omega_{\mathrm{cp}}$, and $\nu_T t_e = 1/4$ (Hellinger and Trávníček 2010) is shown in Figure 8 which displays on the top left panel the (solid) path in the space $(\beta_{\mathrm{p}\parallel}, T_{\mathrm{p}\perp}/T_{\mathrm{p}\parallel})$ compared to bi-Maxwellian kinetic linear predictions, isocontours of the maximum growth rate being equal to $10^{-3}\omega_{\mathrm{cp}}$ as functions of $\beta_{\mathrm{p}\parallel}$ and $T_{\mathrm{p}\perp}/T_{\mathrm{p}\parallel}$ for the (dashed) parallel fire hose and the (dash-dotted) oblique fire hose. The dash-dot-dot-dotted line displays the collisional theoretical prediction. The top right panel shows the fluctuating magnetic energy $\delta B^2/B_0^2$ as a function of R, the bottom left panel shows the fluctuating magnetic energy $\delta B^2/B_0^2$ as a function of R and wave vector k, and the bottom right panel shows fluctuating magnetic energy $\delta B^2/B_0^2$ as a function of R and the angle between the wave vector k and the ambient magnetic field θ_{kB}.

According to Eqs. (2) and (5), the simulated ideal slow expansion (for the assumed strictly radial magnetic field) generates a continuous decrease of the proton temperature anisotropy $T_{\mathrm{p}\perp}/T_{\mathrm{p}\parallel}$ as well as a continuous increase of $\beta_{\mathrm{p}\parallel}$ as long as the system is stable. Then, the system becomes unstable first with respect to the dominant parallel fire hose. This instability generates low-frequency, ion whistler waves and their presence makes the evolution to depart from the collisional prediction. The parallel fire hose has a quasi-linear saturation, the whistler waves interact through the anomalous cyclotron resonance with mainly the supra-Alfvénic protons which are minor for $\beta_{\mathrm{p}\parallel} \sim 1$ (Matteini et al. 2006) while the major core protons are nearly double-adiabatic. Consequently, the proton temperature anisotropy $T_{\mathrm{p}\perp}/T_{\mathrm{p}\parallel}$ further decreases and the system becomes unstable with respect to the oblique fire hose instability that efficiently heats the protons and remove the proton anisotropy owing to the self-destructing nonlinear evolution (Hellinger and Matsumoto 2000, 2001). The oblique instability disrupts the quasi-linear balance of the whistler waves and a large portion of whistler wave energy is dissipated to protons; only long-wavelength whistler waves remains in the system as well as long-wavelength Alfvén waves resulting from the inverse cascade. The resulting low wave activity and weak collisions are not able to counteract the anisotropization driven by the expansion the evolution repeats itself. The HEB simulation results indicate that both parallel and oblique proton fire hose

instabilities constrain the proton temperature anisotropy in the expanding solar wind with the latter one constituting a final frontier for the proton temperature anisotropy which explains the apparent discrepancy between the linear prediction and observations for $T_{\mathrm{p}\perp} < T_{\mathrm{p}\parallel}$ in the Wind/SWE data (cf., Figure 1 of Hellinger et al. 2006, and Figure 7).
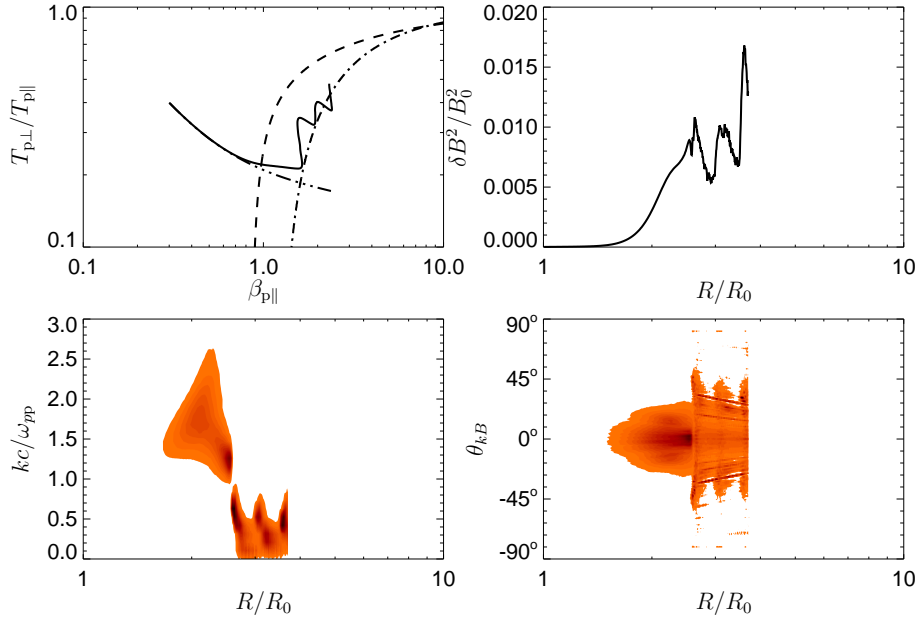

Fig. 8 Results of the weakly collisional HEB simulation (Hellinger and Trávníček 2010): (top left) Path in the space $(\beta_{\mathrm{p}\parallel}, T_{\mathrm{p}\perp}/T_{\mathrm{p}\parallel})$ compared to bi-Maxwellian kinetic linear predictions, isocontours of the maximum growth rate being equal to $10^{-3}\omega_{\mathrm{cp}}$ as a function of $\beta_{\mathrm{p}\parallel}$ and $T_{\mathrm{p}\perp}/T_{\mathrm{p}\parallel}$ for the (dashed) parallel fire hose and the (dash-dotted) oblique fire hose. The dash-dot-dot-dotted line displays the collisional theoretical prediction. (top right) Fluctuating magnetic energy $\delta B^2/B_0^2$ as a function of R. (bottom left) Fluctuating magnetic energy $\delta B^2/B_0^2$ as a function of R and wave vector k. (bottom right) Fluctuating magnetic energy $\delta B^2/B_0^2$ as a function of R and the angle between the wave vector k and the ambient magnetic field θ_{kB}.

The fluctuating wave energy $\delta B^2/B_0^2$ increases with time apart from the oscillatory decreases induced by the oblique fire hose. Similarly, 1-D hybrid expanding box simulations (Matteini et al. 2006), (which allow only the parallel fire hose) exhibit a continuous increase of the fluctuating wave energy $\delta B^2/B_0^2$ with time. These results are compatible with the observation results of Bale et al. (2009) which show enhanced transverse magnetic fluctuations near the marginal stability regions of the two fire hose instabilities at 1 AU. Moreover, they can provide a possible interpretation for the wave power enhancement found by Wicks et al. (2010) in Ulysses data at larger distances, although other mechanisms, like beam instabilities, can also contribute to the local generation of fluctuations in the solar wind plasma.

4.3 Beam instabilities

The differential velocity between the proton core and a beam are the source of free energy for many different electromagnetic instabilities (Gary 1993; Daughton and Gary 1998). The most relevant instabilities are the magnetosonic one propagating parallel with respect to the ambient magnetic field, and Alfvén instabilities propagating obliquely. Analogous instabilities may be driven by alpha particles drifting with respect to the (core) protons. These instabilities require drift velocities of the order of the local Alfvén velocity. Possible instability constraints on the differential velocity between the proton core and beam have been identified in the Helios (Marsch and Livi 1987; Tu et al. 2004) and Ulysses (Goldstein et al. 2000; Goldstein et al. 2010) data sets. Possible instability constraints on the differential velocity between the proton core and alpha particles are also reported in Helios data (Tu et al. 2004). These analyses have however the same problem as we have observed in the case of the proton cyclotron instability influenced by the presence of alpha particles: there are too many parameters that have to be taken into account while essentially only two-dimensional cut/projection plots are comprehensible in exploring the multi-dimensional parameter space.
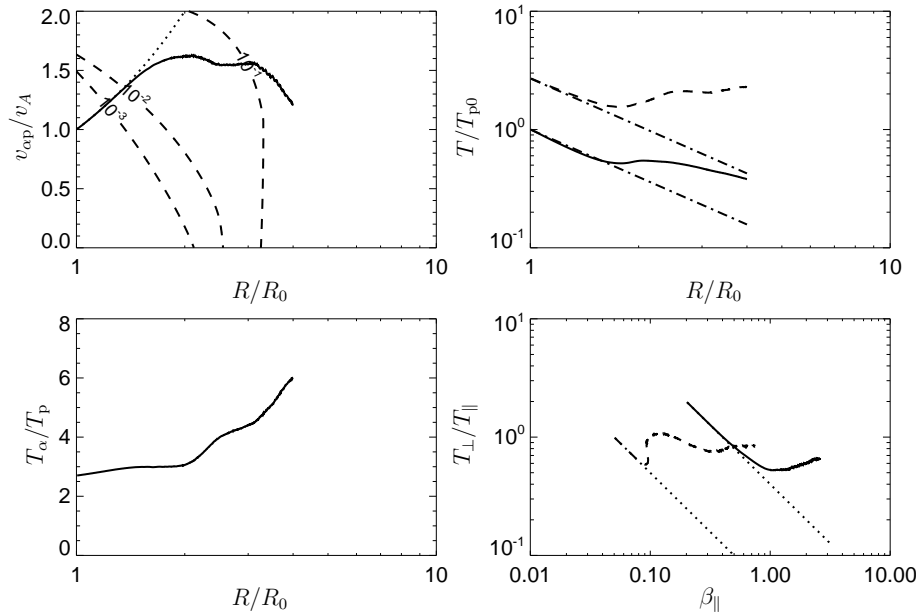
Fig. 9 1-D HEB code for a radial magnetic field: (left top) alpha-proton drift velocity $v_{\alpha p}/v_A$ as a function of R (right top) total (solid) proton and (dashed) alpha temperature T as a function of R, (left bottom) ratio between proton and alpha total temperatures T_α/T_p as a function of R and (right bottom) path in the $(\beta_\parallel, T_\perp/T_\parallel)$ space for protons (solid line) and alpha particles (dashed line). Dash-dotted line in upper left panel shows adiabatic predictions ($T \propto R^{-4/3}$) for the two species and dotted lines show the corresponding CGL predictions. Dashed lines in the left top panels show the contours of the maximum growth rate (in units of ω_{cp}) of the magnetosonic instability as a function of R and the $v_{\alpha p}/v_A$ where the plasma parameters (besides $v_{\alpha p}$) are assumed to follow CGL.

Nonlinear evolution of ion beam driven instabilities are usually studied using the standard hybrid simulations (e.g., Daughton et al. 1999; Li and Lu 2010) starting from the unstable region. These simulations show typically a wave generation inducing a slowing down of the beam with respect to the proton core and a major heating of the beam and a weak heating of the core protons. Hellinger et al. (2003) started to study the role of these instabilities in the expanding solar wind with the strictly radial magnetic field using the HEB code. For a nearly radial magnetic field the CGL predicts a continuous increases of the ratio between the velocity drift and the local Alfvén velocity (see Eq. 6). The HEB simulations of Hellinger et al. (2003) show that the instabilities driven by the alpha-proton drift can bound this drift velocity around the local Alfvén velocity. Here, we consider a remake of the 1-D HEB simulation of Hellinger et al. (2003) with $t_e = 10^4/\omega_{cp}$ and with these initial conditions: $n_p/n_e = 0.9$, $n_\alpha/n_e = 0.05$, $\beta_{p\parallel} = 0.2$, $\beta_{\alpha\parallel} = 0.05$, $T_{p\perp}/T_{p\parallel} = 2$, $T_{\alpha\perp}/T_{\alpha\parallel} = 1$, and $v_{\alpha p} = v_A$ with (R_0 is again assumed to be about 0.3 AU). Results of the simulation are shown in Figure 9. Figure 9 shows (left top) alpha-proton drift velocity $v_{\alpha p}/v_A$ as a function of R, (right top) total (solid) proton and (dashed) alpha temperature T as a function of R, (left bottom) ratio between proton and alpha total temperatures T_α/T_p as a function of R, and (right bottom) path in the $(\beta_\parallel, T_\perp/T_\parallel)$ space for protons (solid line) and alpha particles (dashed line). Dotted lines show the corresponding CGL predictions whereas the dash-dotted line in upper right panel shows adiabatic ($T \propto R^{-4/3}$) predictions. Dashed lines in the left top panels show the contours of the maximum growth rate (in units of ω_{cp}) of the magnetosonic instability as a function of R and $v_{\alpha p}/v_A$ where the plasma parameters (besides $v_{\alpha p}$) are assumed to follow CGL. Figure 9 clearly demonstrates the role of the magnetosonic instability driven by the alpha-proton drift $v_{\alpha p}$: the CGL-predicted increase of $v_{\alpha p}/v_A$ is stopped and alpha particles and protons are heated (see Figure 6 for comparison with the case without instability). At later times the magnetosonic instability becomes the parallel fire hose (cf., Hellinger and Trávníček 2006); this effect explains the contours of the left top panel predicting an instability at $v_{\alpha p} = 0$ which is related to the CGL-predicted strong temperature anisotropy. The parallel fire hose instability leads to a proton isotropization as well as to a significant slowing down of the alpha particles (with respect to protons) and their heating. Similar behavior is also expected for the oblique instabilities and the corresponding proton beam driven instabilities. It is important to note that these instabilities may have a major influence on other (minor) ions (Li and Lu 2010).

5 Cyclotron heating of ions

The solar wind exhibits a strong wave activity on a very large range of spatial and temporal scales. Most of the energy is on large scales while a very efficient transfer of the wave energy to particle appears at short wavelengths through Landau and cyclotron resonances (Hollweg 1999; Hollweg and Isenberg 2002, and references therein). The transfer of energy from large to small scales appears naturally through the turbulent cascade which seems to prefer a cascade to larger perpendicular wave vectors in magnetized plasmas, leading to anisotropic turbulence. At the same time as the cascade, the solar wind expansion brings the wave energy towards particle scales as the ambient magnetic field (and the particle cyclotron frequency) decreases with the distance.

For an undamped, nondispersive and noninteracting Alfvén wave in a slowly expanding plasma the amplitude of fluctuating magnetic field δB is expected to follow

the WKB approximation (Parker 1965; Roberts et al. 1990); assuming the wave action is conserved we have (cf. Liewer et al. 2001; Hellinger et al. 2005):

$$\delta B^2 \propto R^{-3}. \tag{11}$$

Alfvén waves propagating from the Sun encounter decreasing cyclotron frequency till they reach the resonance with ions where they are damped. This effect is the base for the "frequency sweeping scenario" (e.g., Schwartz et al. 1981). This scenario has been first studied using the HEB model by Liewer et al. (2001) investigating proton and alpha particle heating by high-frequency Alfvén waves through the cyclotron resonance. More recently, Hellinger et al. (2005) studied the role of minor heavy ions (Cranmer 2000). Figure 10 shows the HEB simulation result starting with $t_e = 2 \times 10^3/\omega_{cp}$ and $\beta_p = 10^{-2}$, $n_\alpha/n_e = 5 \cdot 10^{-2}$, $\beta_\alpha = 5.5 \cdot 10^{-4}$, $n_{O^{5+}}/n_e = 2 \cdot 10^{-4}$, $\beta_{O^{5+}} = 2.2 \cdot 10^{-6}$. The initial Alfvén cyclotron wave spectrum is flat with the fluctuating magnetic energy $\delta B^2/B_0^2 = 1.25 \times 10^{-3}$ consisting of 50 modes in the wave vector range $0.003 \div 0.153 c/\omega_{pp0}$, far from the cyclotron resonance with the oxygen.

Left panel of Figure 10 shows a color scale plot of the Alfvén cyclotron wave fluctuating magnetic energy δB^2 (normalized to the WKB prediction, Eq. (11)) as a function of R and the wave vector (normalized to the initial proton inertial length c/ω_{pp0}). Overplotted curves show the approximate resonance condition of the cyclotron waves with (dash-dotted) oxygen O^{5+}, (dashed) alpha particles, and (solid) protons. Right panel shows paths in the $(\beta_\|, T_\perp/T_\|)$ space for (dash-dotted) oxygen O^{5+}, (dashed) alpha particles, and (solid) protons. Dash-dotted lines shows the contours of the maximum growth rate (in units of $\omega_{cO^{5+}}$) of the oxygen cyclotron instability. The plasma-wave system initially follows the CGL and WKB predictions. As the system expands each ion species successively becomes resonant with the waves, first the oxygen ions, then the alpha particles and finally the protons. The heating is efficient for oxygen ions, is less important for alpha particles, and is only weak for protons. A small differential oxygen/proton velocity is generated via the Alfvén-cyclotron interaction. This velocity does not seem to be important for saturation, however, the decoupling from the unstable and marginally stable region is probably related to its development. The HEB simulations of Hellinger et al. (2005) show that the oxygen ion behavior corresponds to a "test particle" response which does not significantly affect the response of the more dense alphas and protons, and, on the other hand, the alpha particles have a strong impact on protons since they are dense enough to block the flow of fluctuation energy toward the proton cyclotron resonance.

Sufficiently strong high frequency Alfvén ion cyclotron wave activity may be responsible for perpendicular heating of minor ions, alpha particles and even protons leading to perpendicular temperatures larger than the parallel ones. Kinetic instabilities then constitute natural constrants on possible temperature anisotropies and constrain the heating (section 4.1). The cyclotron interaction may as well explain drift velocities between minor ions and protons which may lead to beam type instabilities (section 4.3).

The heating and acceleration of alpha particles and proton clearly need substantial wave amplitudes. The HEB simulations of Liewer et al. (2001) show indeed that Alfvén cyclotron waves with larger wave amplitudes may efficiently heat and accelerate alpha particles. However, it is unclear if such amplitudes are realistic. Remote observations of the plasma compressibility (Chandran et al. 2009) rules out large Alfvén wave amplitudes except for nearly parallel (incompressible) propagation. Furthermore, large amplitude Alfvén waves are unstable with respect to parametric instabilities.
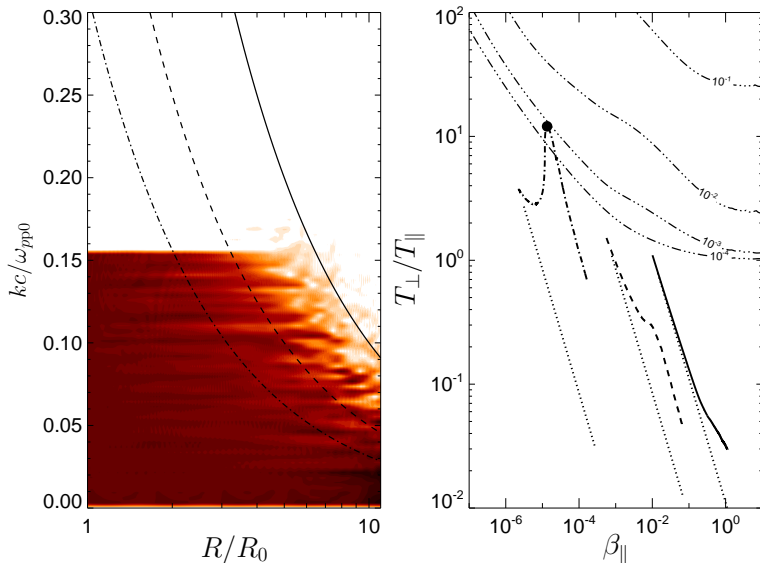
Fig. 10 HEB simulation results (Hellinger et al. 2005): (left) Color scale plot of the Alfvén cyclotron wave fluctuating magnetic energy δB^2 (normalized to the WKB prediction) as a function of R and the wave vector (normalized to the initial proton inertial length c/ω_{pp0}). Overplotted curves show the approximate resonance condition of the cyclotron waves with (dash-dotted) oxygen O^{5+}, (dashed) alpha particles, and (solid) protons. (right) Path in the $(\beta_\parallel, T_\perp/T_\parallel)$ space for (dash-dotted) oxygen O^{5+}, (dashed) alpha particles, and (solid) protons. Dash-dotted lines shows the contours of the maximum growth rate (in units of $\omega_{cO^{5+}}$) of the oxygen cyclotron instability.

6 Parametric instabilities

Parametric instabilities characterize the evolution of nonlinear Alfvén waves (e.g., Lashmore-Davies 1976; Goldstein 1978; Longtin and Sonnerup 1986; Malara and Velli 1996; Del Zanna et al. 2001). They predict the coupling of Alfvénic fluctuations with compressive modes, that lead to the damping of the mother Alfvén wave and the excitation of both Alfvénic and acoustic-like daughter waves. Kinetic effects can play an important role in the dynamics of the parametric instabilities; ion kinetics influences both the growth rate and the range of unstable modes (Inhester 1990; Araneda et al. 2007; Nariyuki et al. 2007). Moreover, when the feedback of the instability on ions is retained, a deformation of their distribution function is observed. It has recently been found that the electric field supported by ion-acoustic fluctuations driven by a modulational (Araneda et al. 2008, 2009) and a decay (Matteini et al. 2010a,2010c) parametric instability can accelerate a fraction of the proton distribution function forming eventually a secondary/beam population. In the presence of an extended spectrum of fluctuations the dynamics becomes more complex and modulational effects of the envelope of the magnetic field can also play a role (Matteini et al. 2010a; Nariyuki et al. 2010); even in this framework the coupling with density fluctuations and the enhancement of the associated electric field can generate a secondary/beam proton population (e.g., Valentini et al. 2008).

Different issues can be investigated varying the many parameters that describe the parametric couplings; on top of the plasma parameters, there are parameters of the
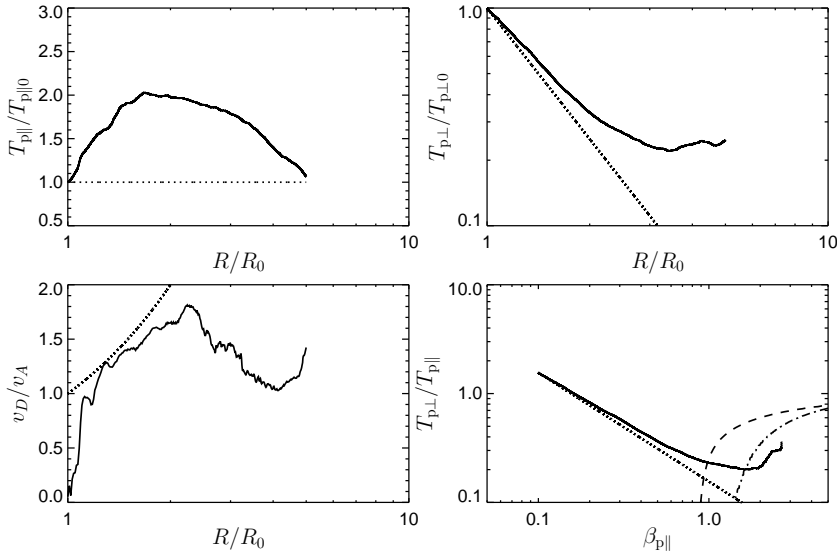
Fig. 11 Evolution in 1-D HEB simulation with an initial spectrum of Alfvén waves: Top panels report the proton parallel (left) and perpendicular (right) temperature profiles. Bottom left panels show the velocity v_D of the secondary proton beam with respect to the core. Bottom right panel reports the evolution as a path in $(\beta_{\mathrm{p}\parallel}, T_{\mathrm{p}\perp}/T_{\mathrm{p}\parallel})$ space; for comparison the theoretical thresholds for (dashed) the parallel fire hose and (dash-dotted) the oblique fire hose are also displayed. Dotted line encodes the corresponding CGL predictions, Eq. (1)
.

wave spectrum. Some aspects about the role of cyclotron heating in the shaping of proton distribution functions in the solar wind are studied with the HEB model in Matteini et al. (2010b). Here we discuss properties of the beam generation and its evolution with the distance.

Figure 11 reports the evolution of protons for 1-D HEB simulation in the presence of an initial Alfvén wave spectrum and $t_e = 10^3/\omega_{c\mathrm{p}}$. The simulation starts with $\beta_{\mathrm{p}\parallel} = 0.1$ and $T_{\mathrm{p}\perp} = 1.5 T_{\mathrm{p}\parallel}$ to reproduce conditions similar to Helios observations at 0.3 AU (Figure 3) but, initially, there is no secondary beam population. The initial spectrum is composed of 40 modes ranging from $k = 0.1$ to $0.4 c/\omega_{p\mathrm{p}0}$ and with the amplitudes $\delta B/B_0 = 5 \cdot 10^{-2}$ for each mode. The chosen wave amplitudes are relatively high and provide a spatial modulation of the initial magnetic field that leads to a faster evolution of the coupling with the density fluctuations and the enhancement of the associated parallel electric field. Top panels of Figure 11 report the proton parallel (left) and perpendicular (right) temperature profiles (solid line). During the first phase of the simulation we observe an increase of the total parallel temperature; at the same time Alfvén waves are observe to decay through parametric interactions and as a result a proton beam drifting along the magnetic field is generated (Figure 12, left panel). This phase of the expansion is also characterized by a perpendicular heating through the cyclotron interaction of the Alfvén wave spectrum with protons. This heating leads to a weak departure of $T_{\mathrm{p}\perp}$ from the double-adiabatic prediction (dotted line). Bottom left panel of Figure 11 shows the drift velocity v_D between the produced proton beam and the proton core (normalized to the local Alfvén velocity v_A). The drift velocity v_D is calculated by fitting the reduced proton velocity distribution function $f_{\mathrm{p}}(v_\parallel)$
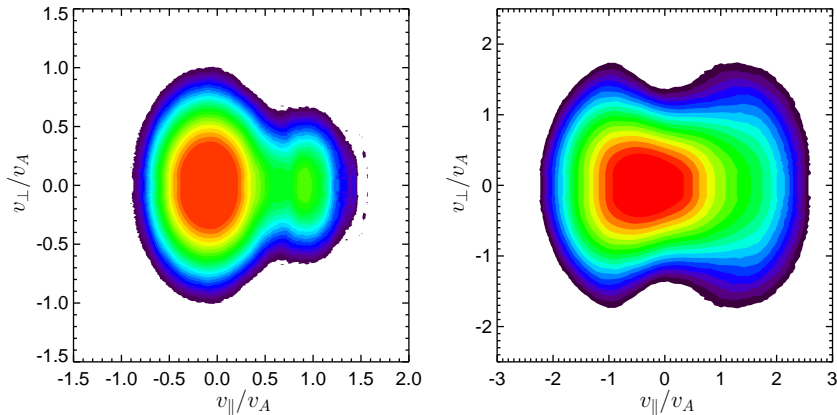
Fig. 12 Results of 1-D HEB simulation with an initial spectrum of Alfvén waves: Proton velocity distribution functions at two simulation times, (left) at $t = 0.4t_e$ ($R = 1.4R_0$) and (right) at $t = 2.5t_e$ ($R = 3.5R_0$) as functions of $v_\parallel$ and $v_\perp$.

by two Maxwellian distribution functions. First, the beam is generated through the parametric instability rapidly creating an important drift velocity $v_D \sim v_A$. Then, v_D/v_A is observed to increase with the distance in a qualitative agreement with the CGL prediction (dotted line). Later on, when the drift velocity reaches $v_D \sim 1.8v_A$, the beam magnetosonic instability takes place. Consequently, protons are diffused by waves excited by the instability and the total parallel temperature begins to decrease. The free energy for the instability also decreases and analogously to the case reported in Figure 9 for the alpha/proton drift, the drift of the secondary proton population with respect to the core protons is reduced. Finally, bottom right panel reports the evolution of the plasma as a path in the $(\beta_{p\parallel}, T_{p\perp}/T_{p\parallel})$ space. At the final stage of the simulation the distribution becomes unstable to a parallel fire hose instability which provides a large perpendicular heating and reduces further the parallel temperature. Note that the proton beam-core velocity distribution function significantly differs from a bi-Maxwellian one. Consequently, the agreement between the simulation results and the parallel fire hose instability threshold predicted by the bi-Maxwellian linear theory (Figure 11, bottom right panel, dashed line) is only qualitative.

Figure 12 reports the proton velocity distribution function at two simulation times (left) $t = 0.4t_e$ and (right) $t = 2.5t_e$. At $t = 0.4t_e$ corresponding to $R = 1.4R_0$ the proton beam formed through the Landau resonance between protons and ion-acoustic fluctuation driven by the parametric instability of the initial Alfvén wave spectrum. At a later time $t = 2.5t_e$ ($R = 3.5R_0$) the distribution is reshaped through the diffusion by the waves excited by the magnetosonic instability. This interaction leads to the heating of the distribution function (Daughton et al. 1999) which occurs preferentially in the direction perpendicular to the magnetic field for both the core and the beam population. This picture confirms that, as suggested by Schwartz et al. (1981), the presence of a proton beam drift can be the source for anisotropic ion heating in the solar wind.

7 Discussion

We have presented selected relevant examples of the ion kinetic process in the solar wind. We have focused our analysis on the role of expansion; the solar wind is not a simply static plasma and its expansion induces changes in the characteristic wave and particle scales. Distribution functions are then characterized by non-thermal features and the evolution of the plasma is not trivial; even the effects of Coulomb collisions for particles far from thermal equilibrium is complicated.

Coulomb collisions tend to reduce temperature anisotropies and relative particle velocities. While the asymptotic stage of Coulomb collisions is characterized by one velocity and one isotropic temperature, at intermediate times they may lead to (anisotropic) preferential heating of drifting ion populations. The role of collisions depends on the solar wind properties and varies with the distance and latitude. In the slow wind, which is denser and cooler, they are more effective in removing ion anisotropies and the relative proton-alpha drift (see Figure 4), while no clear role of collisions is observed in the fast wind. As discussed in Section 3, the local collisionality factor $\nu_T t_e$ (product of the local collisional frequency and the expansion time), may depend on the magnetic field geometry and, consequently, may depend on the latitude. The local collisionality also strongly depends on the particle temperatures; any heating or cooling may importantly affect the efficiency of collisional coupling.

Kinetic instabilities transform a portion of the free energy (anisotropy, drift velocity) to wave energy and to particle heating (modifications of the particle velocity distribution function). Resonant particles are mostly affected while the non-resonant ones are only weakly influenced. However, the nonresonant heating is not generally negligible especially when the system follows a marginally-stable path and effects of such a heating sum up. Kinetic instabilities driven by ion temperature anisotropies with $T_\parallel > T_\perp$ need substantially large betas ($\beta \sim 1$). Consequently, this kind of processes is expected to play a role at larger distances from the Sun, in agreement with observations that suggest that such instabilities are at work at 1 AU and beyond (e.g., Hellinger et al. 2006; Matteini et al. 2007). On the other side, instabilities driven by the velocity drifts can develop also at $\beta < 1$ (provided that the drift is comparable to the local Alfvén speed), so that they are expected to play a role also at smaller distances from the Sun.

High frequency Alfvén (cyclotron) waves are natural source of perpendicular heating through the cyclotron resonance. The heating is especially efficient for minor ions and alpha particles. Temperature anisotropy driven instabilities with $T_\perp > T_\parallel$ constitute natural constraints on the anisotropic cyclotron heating. The cyclotron resonant heating may also explain faster speeds of minor ions and alpha particles with respect to protons. The cyclotron resonant heating is possibly active from the corona and may be responsible for the ion properties observed at 0.3 AU and beyond. The temperature anisotropy driven instabilities for $T_\perp > T_\parallel$ are likely constraining mechanisms counteracting the perpendicular heating during the solar wind evolution.

Large amplitude Alfvén wave are subject to parametric instabilities, wave-wave interactions with compressible ion-acoustic-like waves. Ion-acoustic-like waves generated by parametric couplings interact with ions through the Landau resonance leading to a significant parallel heating/particle acceleration. The parametric instabilities may be especially relevant at smaller distances from the Sun where $\beta_{\rm p}$ is small which leads to formation of a well-pronounced secondary proton beam population (observed already at 0.3 AU). At larger distances the proton beam can become unstable, leading then to

the perpendicular diffusion of such accelerated particles. Moreover, parametric decay instabilities introduce changes in the predicted evolution of Alfvénic fluxes with distance, generating backward (sunward) propagating waves from an initial anti-sunward flux (e.g., Del Zanna et al. 2001), in qualitative agreement with solar wind observations (Bavassano et al. 2000); they also lead to the direct generation of small scale transverse fluctuations when oblique mother Alfvén waves are considered (Matteini et al. 2010c). These aspects suggest that parametric couplings characterizing the nonlinear evolution of Alfvénic fluctuations, can play an active role in the development and evolution of the solar wind turbulence.

In summary, the presented results show that these kinetic effects can be treated separately only to a first approximation as, really, they are interconnected and controlled by the expansion. Different processes can inhibit or enhance each other. Perpendicular cyclotron heating can make ion distribution unstable and then destabilize $T_\perp > T_\parallel$ temperature anisotropy instabilities which act as limiting processes for the heating itself. On the other hand, $T_\parallel > T_\perp$ instabilities can also reduce/stop the perpendicular cooling driven by the expansion, producing then the opposite effect and injecting wave power into plasma fluctuations (possibly affecting the local properties of energy cascade by turbulence (Bale et al. 2009)). Also, different instabilities share/compete for a same free energy and a source of energy for one instability can be converted into free energy for other instabilities. Wave-wave interactions as parametric coupling can generate velocity beams in the proton velocity distribution functions. Such beams can be driven unstable as the Alfvén velocity decreases owing to the expansion; the reduction of the alpha or secondary proton drifts by those instabilities can then constitute a supplementary source for anisotropic plasma heating, competitive to other sources of heating, as turbulent heating. While the presence of a developed turbulent spectrum of fluctuations is a well established observational result, the role of turbulence in the global solar wind plasma evolution still presents many open questions. Solar wind turbulence shows apparent signature of anisotropy; observations (e.g., Horbury et al. 2008) show that the energy cascade evolves preferentially through perpendicular wave vectors, but how these interact with particles is not well understood. Also, recent studies (Sahraoui et al. 2009; Alexandrova et al. 2009) suggest that the range of solar wind turbulence, from large-MHD to small-kinetic scales, continues beyond the ion regime, reaching smaller scales and that dissipation then occurs at electronic scales. Although this picture is in agreement with theoretical models (e.g., Schekochihin et al. 2009; Gary and Smith 2009), it is unclear how much of the cascading energy is then deposited on ions and how (parallel versus perpendicular heating, resonant versus non-resonant process, etc.). It is necessary to fully understand the role of the relevant processes discussed in this review and their influence on the ion energetics in order to better constrain the role of turbulent heating (e.g., Vasquez et al. 2007; Cranmer et al. 2009). The global energy exchanges between waves/turbulence and particles are complicated and further work including all the relevant effects is needed in order to describe the full complexity of the solar wind ion kinetics.

A Glossary

Here $\perp$ and $\parallel$ denote the directions with respect to the ambient magnetic field $\mathbf{B}_0$, $B_0 = |\mathbf{B}_0|$ denotes its the magnitude; $\mathbf{v}$ (and $\mathbf{u}$) denotes a velocity, $v = |\mathbf{v}|$ being its magnitude, and $v_\parallel$ and $v_\perp$ denote magnitude of the velocity components parallel and perpendicular to $\mathbf{B}_0$, respectively; t denotes the time. Here subscripts s denotes different species; p stands

for protons,α for alpha particles; subscript 0 denotes the initial value. $T_{s\perp}$ and $T_{s\parallel}$ denote the perpendicular and parallel temperatures, respectively, and $\beta_{s\parallel} = 2\mu_0 n_s k_B T_{s\parallel}/B_0^2$ is the parallel beta. Here $\omega_{cs} = q_s B_0/m_s$ and $\omega_{ps} = (n_s q_s^2/m_s \epsilon_0)^{1/2}$ denote the cyclotron and plasma frequencies, respectively, $v_{ths\parallel} = (k_B T_{s\parallel}/m_s)^{1/2}$ and $v_{ths\perp} = (k_B T_{s\perp}/m_s)^{1/2}$ denote the parallel and perpendicular thermal velocities. In these expressions m_s, q_s, and n_s denote the mass, the charge, and the number density, respectively (the proton charge is $q_p = e$); ϵ_0 and μ_0 denote the vacuum electric permittivity and magnetic permeability, respectively; k_B is Boltzmann constant. Here $\ln \Lambda$ stands for the (proton-proton) Coulomb logarithm. Here v_{sw} denotes the solar with velocity, R is the radial distance from the Sun, $v_{s\parallel}$ is the mean velocity, $v_{\alpha p}$ is the alpha-proton drift velocity $v_{\alpha p} = v_{\alpha \parallel} - v_{p\parallel}$, v_D is the drift velocity between the proton bean and core. Here δB denotes the magnitude of the fluctuating magnetic field. t_e is the characteristic expansion time $t_e = R/v_{sw}$. Here ν_T is the proton collisional isotropization frequency whereas ν_V is the collisional slowing down frequency between alpha particles and protons.

References

O. Alexandrova, J. Saur, C. Lacombe, A. Mangeney, J. Mitchell, S.J. Schwartz, P. Robert Phys. Rev. Lett. **103**, 165003 (2009)

J.A. Araneda, Y. Maneva, E. Marsch Phys. Rev. Lett. **102**, 175001 (2009)

J.A. Araneda, E. Marsch, A. F.-Viñas Phys. Rev. Lett. **100**, 125003 (2008)

J.A. Araneda, E. Marsch, A.F. Viñas J. Geophys. Res. **112**, A04104 (2007). doi: 10.1029/2006JA011999

S.D. Bale, J.C. Kasper, G.G. Howes, E. Quataert, C. Salem, D. Sundkvist Phys. Rev. Lett. **103**, 211101 (2009)

A.R. Barakat, R.W. Schunk J. Phys. D: Appl. Phys. **14**, 421–438 (1981)

B. Bavassano, E. Pietropaolo, R. Bruno J. Geophys. Res. **105**, 15959–15964 (2000)

S.I. Braginskii, Transport processes in plasmas, in *Reviews of Plasma Physics*, vol. 1, ed. by M.A. Leontovich vol. 1 (Consultants Bureau, New York, 1965), pp. 205–311

E. Camporeale, D. Burgess J. Geophys. Res. **113**, A07107 (2008). doi:10.1029/2008JA013043

B.D.G. Chandran, E. Quataert, G.G. Howes, Q. Xia, P. Pongkitiwanichakul Astrophys. J. **707**, 1668–1675 (2009)

G.F. Chew, M.L. Goldberger, F.E. Low Proc. Roy. Soc. London **236**, 112 (1956)

S.R. Cranmer Astrophys. J. **532**, 1197–1208 (2000)

S.R. Cranmer, W.H. Matthaeus, B.A. Breech, J.C. Kasper Astrophys. J. **702**, 1604–1614 (2009)

W. Daughton, S.P. Gary J. Geophys. Res. **103**, 20613–20620 (1998)

W. Daughton, S.P. Gary, D. Winske J. Geophys. Res. **104**, 4657–4668 (1999)

L. Del Zanna, M. Velli, P. Londrillo Astron. Astrophys. **367**, 705–718 (2001)

S.P. Gary, *Theory of space plasma microinstabilities* (Cambridge Univ. Press, New York, 1993)

S.P. Gary, C.D. Madland J. Geophys. Res. **90**, 7607–7610 (1985)

S.P. Gary, C.W. Smith J. Geophys. Res. **114**, A12105 (2009). doi:10.1029/2009JA014525

S.P. Gary, B.E. Goldstein, J.T. Steinberg J. Geophys. Res. **106**, 24955–24964 (2001)

S.P. Gary, R.M. Skoug, C.W. Smith Phys. Plasmas **12**, 056501 (2005)

S.P. Gary, L. Yin, D. Winske J. Geophys. Res. **111**, A06105 (2006). doi:10.1029/2005JA011552

S.P. Gary, E. Neagu, R.M. Skoug, B.E. Goldstein J. Geophys.Res. **104**, 19843–19850 (1999)

B.E. Goldstein, M. Neugebauer, X. Zhou, in *Twelfth International Solar Wind Conference*, ed. by M. Maksimovic, K. Issautier, N. Meyer-Vernet, M. Moncuquet, & F. Pantellini. AIP Conf. Proc., vol. 1216 (AIP, Melville, New York, 2010), pp. 261–264

B.E. Goldstein, M. Neugebauer, L.D. Zhang, S.P. Gary Geophys. Res. Lett. **27**, 53–56 (2000)

M.L. Goldstein Astrophys. J. **219**, 700–704 (1978)

R. Grappin, M. Velli, A. Mangeney Phys. Rev. Lett. **70**, 2190–2193 (1993)

P. Hellinger, H. Matsumoto J. Geophys. Res. **105**, 10519–10526 (2000)

P. Hellinger, H. Matsumoto J. Geophys. Res. **106**, 13215–13218 (2001)

P. Hellinger, P. Trávníček J. Geophys. Res. **110**, A04210 (2005). doi:10.1029/2004JA010687

P. Hellinger, P. Trávníček J. Geophys. Res. **111**, A01107 (2006). doi:10.1029/2005JA011318

P. Hellinger, P.M. Trávníček J. Geophys. Res. **113**, A10109 (2008). doi:10.1029/2008JA013416

P. Hellinger, P.M. Trávníček Phys. Plasmas **16**, 054501 (2009)

P. Hellinger, P.M. Trávníček J. Comput. Phys. **229**, 5432–5439 (2010)

P. Hellinger, P. Trávníček, A. Mangeney, R. Grappin Geophys. Res. Lett. **30**, 1211 (2003). doi:10.1029/2002GL016409

P. Hellinger, M. Velli, P. Trávníček, S.P. Gary, B.E. Goldstein, P.C. Liewer J. Geophys. Res. **110**, A12109 (2005). doi:10.1029/2005JA011244

P. Hellinger, P. Trávníček, J.C. Kasper, A.J. Lazarus Geophys. Res. Lett. **33**, L09101 (2006). doi:10.1029/2006GL025925

M. Heuer, E. Marsch J. Geophys. Res. **112**, A03102 (2007). doi:10.1029/2006JA011979

J.V. Hollweg J. Geophys. Res. **104**, 24781–24792 (1999)

J.V. Hollweg, P.A. Isenberg J. Geophys. Res. **107**, 1147 (2002). doi:10.1029/2001JA000270

T.S. Horbury, M. Forman, S. Oughton Phys. Rev. Lett. **101**, 175005 (2008)

B. Inhester J. Geophys.Res. **95**, 10525–10539 (1990)

J.C. Kasper, A.J. Lazarus, S.P. Gary Geophys. Res. Lett. **29**, 1839 (2002). doi:10.1029/2002GL015128

J.C. Kasper, A.J. Lazarus, S.P. Gary Phys. Rev. Lett. **101**, 261103 (2008)

J.C. Kasper, A.J. Lazarus, J.T. Steinberg, K.W. Ogilvie, A. Szabo J. Geophys. Res. **111**, A03105 (2006). doi:10.1029/2005JA011442

V.I. Kogan, in *Plasma Physics and the Problem of Controlled Thermonuclear Reactions*, vol. 1, ed. by M.A. Leontovich. (Pergamon Press, New York, 1961), pp. 153–161

J.L. Kohl et al. Astrophys. J. **501**, 127–131 (1998)

S. Landi, F.G.E. Pantellini Astron. Astrophys. **372**, 686–701 (2001)

S. Landi, F.G.E. Pantellini Astron. Astrophys. **400**, 769–778 (2003)

S. Landi, F. Pantellini, L. Matteini, in *Twelfth International Solar Wind Conference*, ed. by M. Maksimovic, K. Issautier, N. Meyer-Vernet, M. Moncuquet, & F. Pantellini. AIP Conf. Proc., vol. 1216 (AIP, Melville, New York, 2010), pp. 218–222

C.N. Lashmore-Davies Phys. Fluids **19**, 587–589 (1976)

J. Lemaire, M. Scherer J. Geophys.Res. **76**, 7479–7490 (1971)

X. Li, S.R. Habbal J. Geophys. Res. **105**, 27377–27386 (2000)

X. Li, Q.M. Lu J. Geophys. Res. **115**, A08105 (2010). doi:10.1029/2010JA015303

X. Li, S.R. Habbal, J. Kohl, G. Noci Astrophys. J. **501**, 133–137 (1998)

P.C. Liewer, M. Velli, B.E. Goldstein J. Geophys. Res. **106**, 29261–29282 (2001)

S. Livi, E. Marsch Ann. Geophys. **4**, 333–340 (1986)

S. Livi, E. Marsch J. Geophys. Res. **92**, 7255–7261 (1987)

S. Livi, E. Marsch, H. Rosenbauer J. Geophys. Res. **91**, 8045–8050 (1986)

M. Longtin, B.U.O. Sonnerup J. Geophys. Res. **91**, 6816–6824 (1986)

F. Malara, M. Velli Phys. Plasmas **3**, 4427–4433 (1996)

E. Marsch Living Rev. Solar Phys. **3** (2006). http://www.livingreviews.org/lrsp-2006-1

E. Marsch, S. Livi J. Geophys. Res. **92**, 7263–7268 (1987)

E. Marsch, X.Z. Ao, C.Y. Tu J. Geophys. Res. **109**, A04102 (2004). doi:10.1029/2003JA010330

E. Marsch, L.E. Zhao, C.Y. Tu Ann. Geophys. **24**, 2057–2063 (2006)

E. Marsch, H. Rosenbauer, R. Schwenn, K.H. Muehlhaeuser, F.M. Neubauer J. Geophys. Res. **87**, 35–51 (1982a)

E. Marsch, R. Schwenn, H. Rosenbauer, K.H. Muehlhaeuser, W. Pilipp, F.M. Neubauer J. Geophys. Res. **87**, 52–72 (1982b)

B. Maruca, J.C. Kasper, S.P. Gary, A.J. Lazarus, A. Szabo, Direct evidence of instability-driven constraints on helium temperature anisotropies in the solar wind, AGU Fall meeting, abstract SH51C-05 (2009)

L. Matteini, S. Landi, P. Hellinger, M. Velli J. Geophys. Res. **111**, A10101 (2006). doi:10.1029/2006JA011667

L. Matteini, S. Landi, P. Hellinger, F. Pantellini, M. Maksimovic, M. Velli, B.E. Goldstein, E. Marsch Geophys. Res. Lett. **34**, L20105 (2007). doi:10.1029/2007GL030920

L. Matteini, S. Landi, M. Velli, P. Hellinger J. Geophys. Res. **115**, A09106 (2010a). doi: 10.1029/2009JA014987

L. Matteini, S. Landi, M. Velli, P. Hellinger, in *Twelfth International Solar Wind Conference*, ed. by M. Maksimovic, K. Issautier, N. Meyer-Vernet, M. Moncuquet, & F. Pantellini. AIP Conf. Proc., vol. 1216 (AIP, Melville, New York, 2010b), pp. 223–226

L. Matteini, S. Landi, L. Del Zanna, M. Velli, P. Hellinger Geophys. Res. Lett. **37**, L20101 (2010c). doi:10.1029/2010GL044806

A.P. Matthews J. Comput. Phys. **112**, 102–116 (1994)

Y. Nariyuki, T. Hada, K. Tsubouchi Phys. Plasmas **14**, 122110 (2007)

Y. Nariyuki, T. Hada, K. Tsubouchi Phys. Plasmas **17**, 072301 (2010)

E.N. Parker Astrophys. J. **128**, 664–676 (1958)

E.N. Parker Space Sci. Rev. **4**, 666–708 (1965)

J.L. Phillips, J.T. Gosling J. Geophys. Res. **95**, 4217–4228 (1990)

V. Pierrard, K. Issautier, N. Meyer-Vernet, J. Lemaire Geophys. Res. Lett. **28**, 223–226 (2001)

C.P. Price, D.W. Swift, L.C. Lee J. Geophys. Res. **91**, 101–112 (1986)

D.A. Roberts, M.L. Goldstein, L.W. Klein J. Geophys. Res. **95**, 4203–4216 (1990)

F. Sahraoui, M.L. Goldstein, P. Robert, Y.V. Khotyaintsev Phys. Rev. Lett. **102**, 231102 (2009)

C. Salem, D. Hubert, C. Lacombe, S.D. Bale, A. Mangeney, D.E. Larson, R.P. Lin Astrophys. J. **585**, 1147–1157 (2003)

A.A. Schekochihin, S.C. Cowley, W. Dorland, G.W. Hammett, G.G. Howes, E. Quataert, T. Tatsuno Astrophys. J **182**, 310–377 (2009)

M. Schulz, A. Eviatar J. Geophys. Res. **78**, 3948–3951 (1973)

S.J. Schwartz, W.C. Feldman, S.P. Gary J. Geophys. Res. **86**, 541–546 (1981)

L. Spitzer, R. Härm Phys. Rev. **89**, 977–981 (1953)

D. Telloni, E. Antonucci, M.A. Dodero Astron. Astrophys. **476**, 1341–1346 (2007)

C.Y. Tu, E. Marsch, Z.R. Qin J. Geophys. Res. **109**, A05101 (2004). doi: 10.1029/2004JA010391

Š. Štverák, P. Trávníček, M. Maksimovic, E. Marsch, A.N. Fazakerley, E.E. Scime J. Geophys.Res. **113**, A03103 (2008). doi:10.1029/2007JA012733

F. Valentini, P. Veltri, F. Califano, A. Mangeney Phys. Rev. Lett. **101**, 025006 (2008)

B.J. Vasquez, C.W. Smith, K. Hamilton, B.T. MacBride, R.J. Leamon J. Geophys. Res. **112**, A07101 (2007). doi:10.1029/2007JA012305

M.K. Verma, D.A. Roberts, M.L. Goldstein J. Geophys. Res. **100**, 19839–19850 (1995)

R.T. Wicks, T.S. Horbury, C.H.K. Chen, A.A. Schekochihin Mon. Not. R. Astron. Soc. **407**, 31–35 (2010)

L.L. Williams, G.P. Zank, W.H. Matthaeus J. Geophys. Res. **100**, 17059–17068 (1995)

I. Zouganelis, N. Meyer-Vernet, S. Landi, M. Maksimovic, F. Pantellini Astrophys. J. **626**, 117–120 (2005)